A Micromegas-based low-background x-ray detector coupled to a slumped-glass telescope for axion research

JCAP12(2015)008

(http://iopscience.iop.org/1475-7516/2015/12/008)

Journal of Cosmology and Astroparticle Physics
An IOP and SISSA journal

A Micromegas-based low-background x-ray detector coupled to a slumped-glass telescope for axion research

F. Aznar,[a,1] **J. Castel,**[a] **F.E. Christensen,**[b] **T. Dafni,**[a,2] **T.A. Decker,**[c] **E. Ferrer-Ribas,**[d] **J.A. Garcia,**[a] **I. Giomataris,**[d] **J.G. Garza,**[a] **C.J. Hailey,**[e] **R.M. Hill,**[c] **F.J. Iguaz,**[a] **I.G. Irastorza,**[a] **A.C. Jakobsen,**[b] **G. Luzon,**[a] **H. Mirallas,**[a] **T. Papaevangelou,**[d] **M.J. Pivovaroff,**[c] **J. Ruz,**[c] **T. Vafeiadis**[f] **and J.K. Vogel**[c]

[a]Grupo de Física Nuclear y Astropartículas, Universidad de Zaragoza, C/P. Cerbuna 12 50009, Zaragoza, Spain
[b]DTU Space, National Space Institute, Technical University of Denmark, Elektrovej 327, DK-2800 Lyngby, Denmark
[c]Lawrence Livermore National Laboratory, Livermore, CA 94550, U.S.A.
[d]CEA, IRFU, Centre d'Études Nucléaires de Saclay, Gif-sur-Yvette, France
[e]Physics Department and Columbia Astrophysics Laboratory, Columbia University, New York, NY 10027, U.S.A.
[f]Aristotle University of Thessaloniki, 54124 Thessaloniki, Greece

E-mail: faznar@unizar.es, jfcastel@unizar.es, finn@space.dtu.dk, tdafni@unizar.es, decker4@llnl.gov, esther.ferrer-ribas@cea.fr, jagarpas@unizar.es, ioanis.giomataris@cern.ch, jgraciag@unizar.es, chuckh@astro.columbia.edu, runnemrand@yahoo.com, iguaz@unizar.es, igor.irastorza@cern.ch, jakobsen@space.dtu.dk, luzon@unizar.es, mirallas@unizar.es, thomas.papaevangelou@cea.fr, pivovaroff1@llnl.gov, ruzarmendari1@llnl.gov, Theodoros.Vafeiadis@cern.ch, vogel9@llnl.gov

Received September 22, 2015
Accepted November 10, 2015
Published December 3, 2015

[1]Present address: Centro Universitario de la Defensa, Universidad de Zaragoza. Ctra. de Huesca s/n, 50090, Zaragoza, Spain.
[2]Corresponding author.

doi:10.1088/1475-7516/2015/12/008

JCAP12(2015)008

Abstract. We report on the design, construction and operation of a low background x-ray detection line composed of a shielded Micromegas detector of the microbulk technology. The detector is made from radiopure materials and is placed at the focal point of a $\sim 5\,\mathrm{cm}$ diameter, 1.5 m focal-length, cone-approximation Wolter I x-ray telescope (XRT) assembled from thermally-formed (or "slumped") glass substrates deposited with multilayer coatings. The system has been conceived as a technological pathfinder for the future International Axion Observatory (IAXO), as it combines two of the techniques (optic and detector) proposed in the conceptual design of the project. It is innovative for two reasons: it is the first time an x-ray optic has been designed and fabricated specifically for axion research, and the first time a Micromegas detector has been operated with an x-ray optic. The line has been installed at one end of the CERN Axion Solar Telescope (CAST) magnet and is currently looking for solar axions. The combination of the XRT and Micromegas detector provides the best signal-to-noise ratio obtained so far by any detection system of the CAST experiment with a background rate of 5.4×10^{-3} counts per hour in the energy region-of-interest and signal spot area.

Keywords: axions, dark matter detectors, dark matter experiments, X-ray telescopes

ArXiv ePrint: 1509.06190

JCAP12(2015)008

Contents

1 Introduction

Axions appear in very well motivated extensions of the Standard Model (SM) including the Peccei-Quinn mechanism proposed to solve the long-standing strong-CP problem [1–4]. They are pseudoscalar, very light particles that generically couple with two photons [5]. Therefore, axions can convert into photons (and vice versa) in the presence of electromagnetic fields, a process that is sometimes referred to as Primakoff effect [6], in analogy with the pion-photon conversion. They can be produced non-relativistically in the early Universe [7, 8], and thus they are also a favoured candidate to solve the Dark Matter (DM) problem. Like the case of the Weakly Interacting Massive Particles (WIMPs) in supersymmetric theories, axions are appealing due to the fact that they are not an *ad hoc* solution to the DM problem. While WIMPs and axions could each account on their own for all of the DM, several theories [9, 10] favour the possibility of a mixed WIMP-axion DM. In addition, several extensions of the SM (e.g., string theory [11–13]) predict more generic axion-like particles (ALPs). These could also be produced in the early Universe and be part of the DM [14]. Both axions and ALPs are repeatedly invoked to explain a number of poorly understood astrophysical observations (see e.g. [15] and references therein).

Diverse complementary experimental approaches [16] are being employed in the search for axions and ALPs. In particular, axion helioscopes [17] look for axions emitted by the Sun, and therefore do not rely on the assumption of axions being the DM. The emission of axions by the solar core is a robust prediction involving well known solar physics and the Primakoff conversion of plasma photons into axions. Solar axions have ∼keV energies and can convert back into detectable x-ray photons in strong laboratory magnetic fields. The basic layout of an axion helioscope thus requires a powerful magnet coupled to one or more x-ray detectors. When the magnet is aligned with the Sun, an excess of x-rays, compared to the background measured during non-alignment periods, should appear at the exit of the magnet.

JCAP12(2015)008

Currently, the most powerful axion helioscope is the CERN Axion Solar Telescope (CAST), an experiment that has been in operation at CERN for more than a decade. The experiment uses a Large Hadron Collider (LHC) dipole prototype magnet with a magnetic field of up to 9 T over a length of 9.3 m and an aperture of $2 \times 15\,\mathrm{cm}^2$ [18], that is able to follow the Sun for ~ 3 hours per day using an elevation and azimuth drive. CAST originally set an upper limit on the axion-to-photon coupling of $g_{a\gamma}$ (95% CL) $< 8.8 \times 10^{-11}\,\mathrm{GeV}^{-1}$ [19, 20] for axion masses up to 0.02 eV. Using the buffer gas technique [21] the sensitivity was further extended to masses up to ∼1 eV. The average upper limit provided by CAST with ^{4}He (2005–2006) and ^{3}He (2008–2011)is $g_{a\gamma}$ (95% CL) $\lesssim 2.3 \times 10^{-10}\,\mathrm{GeV}^{-1}$ [22, 23] and $g_{a\gamma}$ (95% CL) $\lesssim 3.3 \times 10^{-10}\,\mathrm{GeV}^{-1}$ [24], respectively, with the exact value depending on the pressure setting.

A new collaboration, that includes the authors of this paper, has shown [25] that the helioscope technique can be substantially scaled in size by building a large aperture superconducting magnet, and by extensive use of x-ray focusing optics and low background x-ray detection techniques. This has been the basis for the proposal of a new generation axion helioscope, the International Axion Observatory [15, 26]. IAXO will require the construction of a large superconducting 8-coil, 20-m long toroidal magnet optimized for axion research [27]. Between the coils, the IAXO magnet will accommodate eight 60 cm-diameter bores, each of them equipped with x-ray optics [28] focusing the signal photons into ∼0.2 cm^2 spots that are imaged by ultra-low background Micromegas (MM) x-ray detectors [29, 30]. The magnet will be built into a structure with elevation and azimuth drives that will allow solar tracking for ∼12 hours each day. IAXO will have a signal-to-noise ratio 4−5 orders of magnitude more sensitive to Primakoff solar axions than CAST, a factor that translates to ∼20 more sensitivity to the axion-photon coupling constant $g_{a\gamma}$. That is, this instrument will reach the few $\times 10^{-12}$ GeV^{-1} regime for a wide range of axion masses up to about 0.25 eV.

All the enabling technologies for IAXO exist, and as part of its technical design phase, the project is validating the ability to achieve the required experimental performance by building and characterizing prototype systems. In this paper, we present the design, construction and operation of one of the IAXO technological pathfinders that combines two of the techniques (optics and detectors) proposed in the conceptual design of the project. The x-ray detector system is a shielded Micromegas (micromesh gas structure) detector made from radiopure materials and using the microbulk technique, an evolution of the detectors already used in the past in the CAST experiment. However, in the present configuration the detector is placed at the focal point of a ∼5 cm diameter, 1.5 m focal-length, cone-approximation Wolter I x-ray telescope (XRT) assembled from thermally-formed (or slumped) glass substrates deposited with multilayer coatings. The approach used to make the XRT closely follows that used to make the x-ray telescopes fabricated for NASA's hard x-ray astrophysics NuSTAR satellite [31] and was identified in [25] as one possible method to produce cost-effective, large area x-ray optics with the performance required for IAXO.

Although CAST has already used x-ray focusing optics on one of its four detector lines [32] (one of the spare optics from the ABRIXAS soft x-ray satellite mission), this is the first time an x-ray optic has been designed and built specifically for an axion application. It is also the first time a Micromegas detector is operated with an x-ray optic in an experimental setup. The system was installed in 2014 in one of the CAST magnet ports searching for axions during sunrise and has been acquiring science data in 2015. The combination of the telescope and Micromegas detector provides the best signal-to-noise ratio obtained so far by any detection system of the CAST experiment and has a background rate of 5.4×10^{-3} counts per hour in the signal spot area and in the 2-7 keV energy region-of-interest (RoI).

JCAP12(2015)008

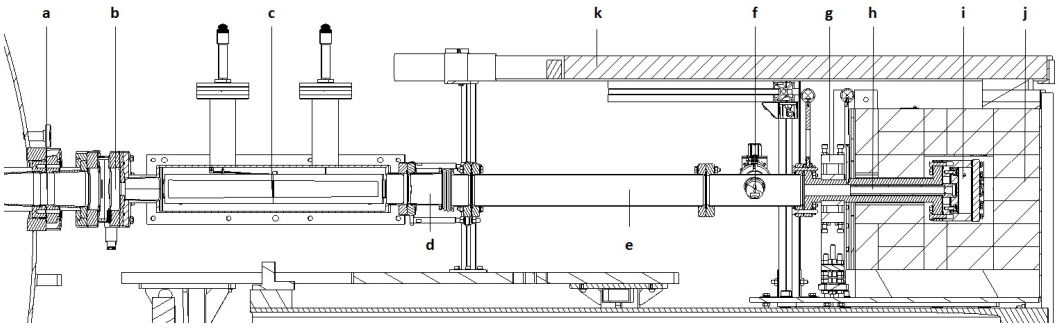

Figure 1. Sketch of the new CAST sunrise detection line composed of a low background Micromegas detector placed at the focal point of an x-ray optic. The different parts of the line are described in detail in the text: (a) gate valve, (b) differential window, (c) Wolter I x-ray optic, (d) bellow, (e) stainless steel interface tube, (f) calibration system, (g) precision stage, (h) copper interface tube, (i) Micromegas detector, (j) lead shielding and (k) muon veto.

In section 2 we give a brief overview of the system, while we describe the x-ray telescope and the x-ray detector in detail in sections 3 and 4, respectively. In section 5, we present the installation and commissioning of the system in CAST, as well as the main performance parameters of the system. Finally, in section 6 we summarize the project and discuss future prospects.

2 Overview of the system

The new line is situated at one of the two CAST sunrise magnet cold bores.[1] It has been designed to fit the dedicated x-ray optic and the low-background Micromegas detector system, and to align the two elements with the magnet bore. Both the optic and the detector have imposed some constraints on the line. On one side, the optic and supporting vacuum elements must fit within a small physical envelope on the existing experimental platform. On the other side, the lead shielding must enclose the detector tightly to effectively reduce the external gamma flux, which limits the range of the alignment elements. A schematic view of the line is shown in figure 1.

Axion-converted x-rays coming from the cold bore would take the following path through the XRT and detector system (for location of single components see figure 1): they pass a *a gate valve*, which isolates the line from the magnet during commissioning periods, and *a differential window* made of 4 μm mylar, which protects the magnet cold bore vacuum in case of a degradation of vacuum on the detector side. *The XRT and its case* are directly bolted to this differential window. Between the Micromegas detector and the optic, there are four elements: *a bellow*, which allows to precisely align the detector with the optic in combination with *a precision stage*; *a stainless steel tube*, whose length roughly fixes the detector position at the optic focal length; *a calibration system*, composed of an actuator with an ^{55}Fe source and *a copper interface tube*, which is screwed to *the detector chamber* and also forms part of the shielding. An octagonal Polytetrafluoroethylene (PTFE) cassette covers the inner tube's

[1] At the CAST experiment, both ends of the magnet are equipped with x-ray detectors, three of which are Micromegas of the microbulk type. The magnet follows the Sun twice a day, during sunrise and during sunset. Depending on whether the detectors are taking data during the sunrise alignment or the sunset one, they are named sunrise Micromegas or sunset Micromegas respectively.

JCAP12(2015)008

walls to block the fluorescence coming from the copper, which might be activated by external radiation. The shielding includes *a lead layer* of 10 cm thickness , which reduces the external gamma flux, and *a plastic scintillator* coupled to a photomultiplier, which works as an active muon veto. The optic and the Micromegas detector are described in detail in the following.

3 Optics

3.1 Overview

The XRT — optimized for operation with the Micromegas detector described below — was designed and fabricated using the same techniques [33–36] developed for the x-ray optics flying on NASA's NuSTAR satellite mission [31]. In this approach, flat-panel glass is thermally formed (slumped) in cylindrical shapes and then cut into truncated cones. After cleaning, the glass substrates are deposited with multilayer coatings to enhance x-ray reflectivity. These individual x-ray reflectors are then glued into a precision assembly that results in a reflective x-ray optic that approximates a Wolter I geometry [37].

For solar axion experiments, x-ray telescopes made from segmented glass substrates offer two distinct advantages, compared to integral-shell telescopes made via replication or from large (ceramic) glass blanks. First, unusual, azimuthally asymmetric designs can be fabricated to minimize the amount of space required for vacuum lines and supporting hardware. This consideration is particularly important for CAST, since during its lifetime, the experiment has undergone several upgrades that have required the addition of new structures. As a result, there is limited space for new instruments, so the use of the segmented-glass fabrication technique was critical in building an x-ray optic with just enough area to cover a single magnet bore that has a diameter of 43 mm. Second, one can deposit multilayer coatings optimized to maximize the x-ray reflectivity exactly at the peak of the axion spectrum, thus increasing the signal-to-noise and sensitivity. This unique advantage is discussed in more detail below.

3.2 Design of the optic

Since the angular size and spectrum of potential solar axion emission is known, it is easy to define a figure of merit that can be used to optimize an x-ray telescope for an axion helioscope [25, 26]. For CAST, the optical design space is limited for several factors. First, the new x-ray optic, Mircomegas detector, vacuum vessels and shielding must fit to the limited physical space available for new instrumentation. This limited the optic to a maximum focal length of 1.5 meters. Another important constraint was the re-use of existing infrastructure originally built for the NuSTAR x-ray telescopes [35, 36]. This sets the minimum radius and defines the length of upper (parabolic-like) and lower (hyperbolic-like) shells. Based on these constraints, a cone-approximation design was generated, compatible with a Micromegas serving as the focal plane and compliant with overall CAST constraints. Table 1 lists the properties of the CAST telescope. The top of figure 2 shows a two-dimensional cross-sectional schematic of the optic, while the bottom of figure 2 shows a simplified ray-trace diagram, a 10:1 stretched view of the XRT focusing parallel light.

The next step was to design the x-ray-reflective multilayer coating, using the general approach discussed in detail in [28]. For this particular optic for CAST, given the limited ability to change optical design parameters, we fixed the material system to Pt/C and restricted the number of coating "recipes" to four. A full explanation of the optimization process is given in [38]. Table 2 presents the key properties of each of the multilayer recipes used for this optic.

JCAP12(2015)008

Property	Value
Mirror substrates	glass, Schott D263
Substrate thickness	0.21 mm
L, length of upper and lower mirrors	225 mm
Overall telescope length	454 mm
f, focal length	1500 mm
Layers	13
Total number of individual mirrors in optic	26
$\rho_{\rm max}$, range of maximum radii	63.24–102.4 mm
$\rho_{\rm mid}$, range of mid-point radii	62.07–100.5 mm
$\rho_{\rm min}$, range of minimum radii	53.85–87.18 mm
α, range of graze angles	0.592–0.968 degrees
Azimuthal extent	Approximately 30 degrees

Table 1. Properties of the segmented-glass telescope at CAST. Refer to figure 2 for more details.

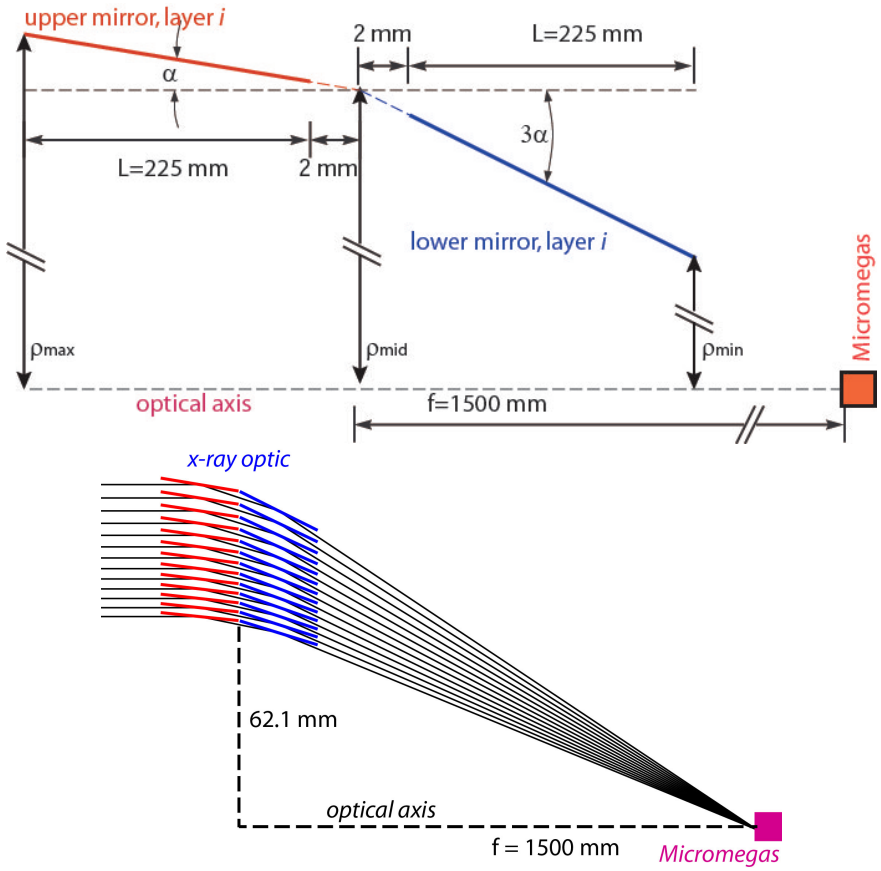

Figure 2. Top: schematic cross-section drawing of the CAST segmented-glass telescope. A single layer i of the telescope is shown, with key dimensions described. Bottom: a 10:1 stretched ray-trace of the optic, where the vertical dimension has been multiplied by a factor of 10 to better show the relative position of the individual mirrors with respect to each other. Each black line represents a single photon, coming from infinity, incident in the middle of each of the 13 nested shells. The cone-approximation Wolter I design focuses all the light to a small region on the Micromegas detector.

JCAP12(2015)008

Design	Applied to layers	N	$d_{\min}$	$d_{\max}$	Γ
1	1–3	2	11.2	22.5	0.46
2	4–6	3	6.9	18.5	0.49
3	7–10	4	5.2	16.2	0.41
4	11–12	5	4.9	13.6	0.40

Table 2. Multilayer coating prescriptions of the Pt/C multilayers.

3.3 Expected CAST performance

The point spread function (PSF) and effective area (EA, or throughput) of the x-ray optic will be calibrated in detail after conclusion of the scientific campaign in late 2015. In the meantime, we have estimated the performance of the optic, as part of the CAST helioscope, based on measurements of the witness samples from the multilayer depositions (for details see [38]), metrology data acquired during the fabrication of the XRT and the in situ measurements with a Cool-X source [39] (see section 5).

To be conservative, we have assumed that the intrinsic figure errors (i.e., long-spatial frequency errors) of the XRT are 1.3 times worse than those achieved for NuSTAR. Once we have calibration data, we will adjust this value to match the measured performance. It is important to note that the performance of the CAST XRT and the NuSTAR x-ray telescopes, however, will not be directly comparable, since one was optimized for solar axion searches, the other for high-angular-resolution astrophysical observations. Specifically, the on-axis PSF of the CAST XRT has extremely large aberrations due to the large ratio of mirror length (225 mm) to the focal length (1500 mm). So while the CAST XRT would make a poor x-ray telescope for general astronomy, it is well-optimized for focusing photons emerging from the central 3 arcminute core of the Sun.

We account for the intrinsic figure errors, extended axion source size, high-spatial frequency errors, in-situ metrology acquired during fabrication, and multilayer reflectivity using ray-tracing software that has been developed and validated for a variety of x-ray applications [40–43]. The very good agreement between the Cool-X data and our simulations indicates that our assumptions are good ones.

To simulate the expected signal spot size, the emission region was modelled as a 3 arcmin diameter, located 1 A.U. from the CAST experiment, and assumed a solar axion differential spectrum given in [20] of the form

$$\frac{d\Phi}{dE} \propto \frac{E^{2.481}}{\exp\left(E/1.205\right)} \,, \tag{3.1}$$

where E is the axion energy in keV.

Millions of photons were ray-traced through the optic, before they were registered on an infinitely large sheet at the focal plane to calculate the telescope throughput (effective area). Figure 3 plots the EA versus energy. It should be noted that this EA is lower than what would be computed using standard practice in the x-ray astronomy community, which reports EA for a point-source on-axis. This approach directly accounts for the loss of throughput and vignetting when imaging an extended source. Finally, a conservative lower energy limit of 1 keV has been set, since no previous calibration of a segmented glass x-ray telescope in the soft x-ray regime exists.

Because the bore only illuminates approximately a 30° azimuthal "wedge" of a surface of revolution, the resultant focused light is not circularly symmetric. For a point-source, the

JCAP12(2015)008

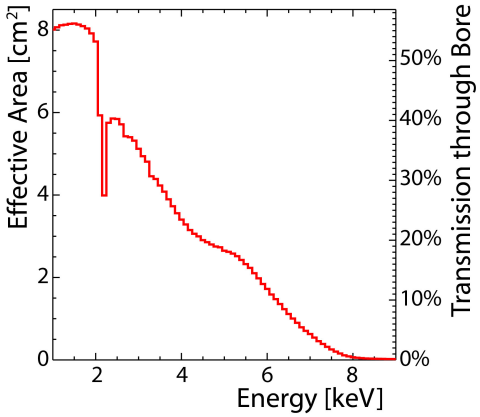

Figure 3. Effective area (cm^2) and transmission (percentage) versus energy. The transmission is computed by dividing the effective area (EA) by the geometric area of the 43 mm diameter bore. The EA was modelled using the as-built optical prescription, assuming a half-power diameter of 75 arcsec and that the solar axion emission comes from a uniformly distributed 3 arcmin disc.

Fraction of the flux captured (%)	Geometric area (mm^2)
47.3	1.44
72.0	3.08
90.6	5.76
99.5	13.6

Table 3. Extraction region sizes and captured flux.

resulting image would resemble a bow-tie. For a source with 3 arcmin angular extent, the focused spot is roughly rectangular. This fact requires the use of rectangular extraction regions, rather than circular extraction regions (e.g., the commonly used half-power diameter). As the extraction regions increase in area, more axion-converted-photons will be captured. Table 3 presents the area of rectangular extraction regions required to enclose increasingly larger fractions of the total reflected signal.

Finally, we restate that our assumption that the CAST XRT has slightly worse figure errors than NuSTAR means these extraction region areas will result in a slightly higher estimate of the background. This conservative step, however, minimizes the risk of missing a putative signal. After the detailed calibration is performed, the analysis can be repeated with smaller extraction regions.

4 Detector

The design of the new detector (figure 4) is the prime example of the current state-of-the-art in low background techniques [29], developed for the Micromegas detectors. In contrast to previous designs [44] the body and the chamber of the detector are made of ∼18 mm thick radiopure copper which has been carefully cleaned; moreover, all the gaskets consist of radiopure PTFE. A new field shaper has also been installed, printed on a kapton circuit and integrated in the chamber. The field shaper, which increases the uniformity of the drift field and reduces border effects, is externally covered by a 3 mm thick PTFE coating in order to

JCAP12(2015)008

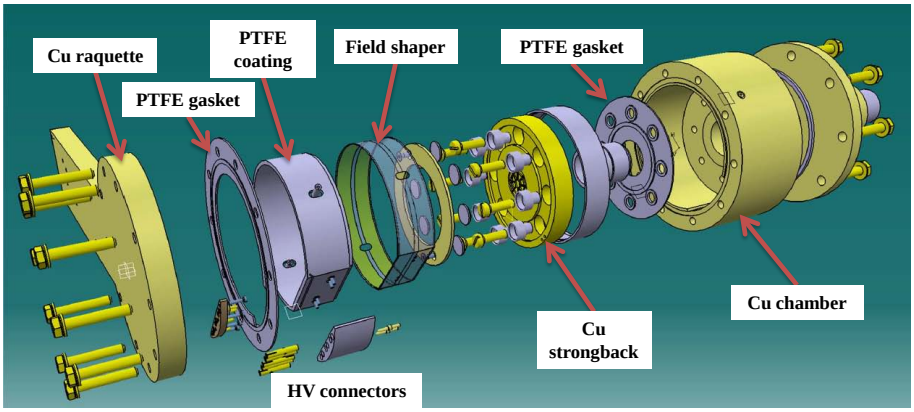

Figure 4. Exploded view of the sunrise Micromegas detector, where the different parts of the chamber are labelled. The components are described in detail in the text.

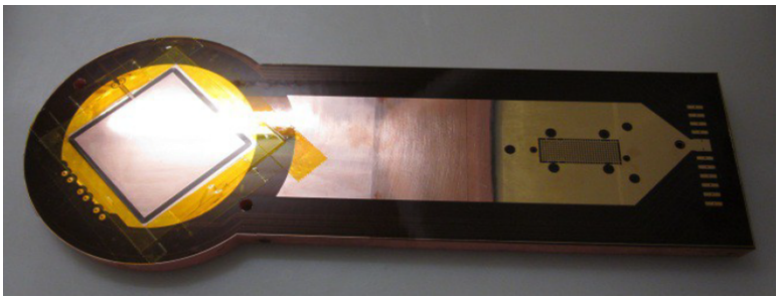

Figure 5. A photograph of the new sunrise Micromegas readout glued on the copper support. At the left of the image is the squared active area, while the strip signals are extracted from a central connector situated on the right part. The high voltage is fed through squared pads situated on the right part and reach the mesh and the field shaper through lines situated at the sides of the printed board.

block copper fluorescence. In addition, the high voltage (HV) connections were implemented in the detector's printed board, allowing for an easy extraction of signal and voltages out of the shielding. A picture of the new Micromegas readout plane is shown in figure 5.

New microbulk-type Micromegas planes have been manufactured for the new line. The readout has been modified with respect to previous versions [45]: the strip pattern has a smaller pitch (500 μm instead of 550 μm) while keeping the same active area (60 $\times$ 60 mm^2), which has increased the number of strips to 120 per axis (as opposed to 109). This new design is the result of studies made on the Micromegas detectors in order to improve their performance and of the enhancements of the manufacturing technique [29]. To date, this is the Micromegas with the best performance used for CAST, achieving a 13% (FWHM) at 5.9 keV (figure 6, left), close to the 11% (FWHM) reached by small non-pixelated microbulk prototypes (3.5 cm diameter) [46]. The detector shows a good gain homogeneity across the active area (figure 6, right).

This improvement in performance is due both to a better manufacturing technique and to the implementation of an optimal ground strategy, described at the end of the section. The electron transmission curve of the detector, which indicates the percentage of primary electrons that will pass from the conversion to the amplification area of the detector through

JCAP12(2015)008

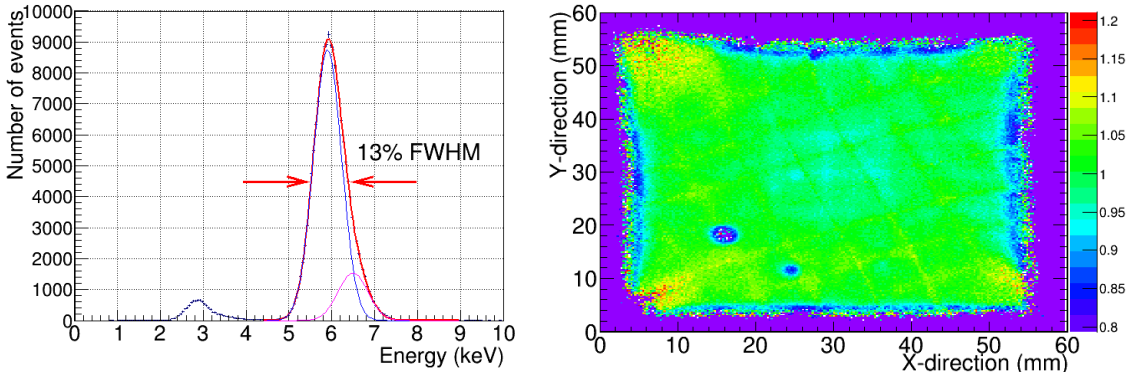

Figure 6. Left: ^{55}Fe calibration spectrum of the sunrise Micromegas detector. The main peak has been fitted to two gaussian functions (blue and magenta lines, in red the sum of them), corresponding to the K_α (5.9 keV) and K_β lines (6.4 keV). Right: gain uniformity of the sunrise Micromegas detector. The dead areas (in purple) show lower values than unity (in green) and lie outside the axion signal area.

the micromesh, depends on the ratio of the fields in the two regions and defines the range of drift fields for an optimum detector performance. In the new detector this range has been enlarged with respect to the previous ones (figure 7, left), owing to a change of the geometry of the micromesh holes (diameter and pitch) and the increased uniformity provided by the field shaper. The gain curve (figure 7, right), mainly defined by the amplification gap and the gas conditions, is similar to previous designs.

The XRT is expected to focus the photons to a spot less than 5 mm in extent. For this reason, the x-ray window (cathode) strongback pattern has been modified to resemble a spider-web design with a central hole of 8.5 mm in diameter, big enough to contain the entire expected axion signal. The focused x-rays go through the 4 μm-thick aluminized polypropylene window avoiding the grid structure, which was responsible for a $\sim$10% of efficiency loss in previous setups. Consequently, the efficiency of the new detector is increased. A photograph of the new strongback design together with its projection during calibrations in the detector are shown in figure 8.

Signals induced both in the mesh and in the strips come out from the active area by printed paths situated in the medium layer of the Micromegas detector. The mesh pulse is subsequently amplified by a CANBERRA 2014 preamplifier and an ORTEC 474 Timing amplifier and then duplicated. One of these copies is then sampled at 1 GHz frequency in a 2.5 μs window and recorded by a 12-bit dynamic range VME digitizing board, MATACQ (MATrix for ACQuisition) [47].

Meanwhile, the strip pulses pass to an interface card, where they are distributed to four flexible cables connected to an AFTER (ASIC For TPC Electronics Readout)-based Front-End Card board [48, 49]. Each one of the four AFTER ASICs collects and samples the strip signals continuously at 100 MHz in 512 samples per channel, recording a window of $\sim$5 μs, which is longer than the maximum drift time of charges created in the active volume. The readout electronics are triggered by the second copy of the mesh pulse. Then, the analogue data from all channels is digitized by an Analog-to-Digital Converter (ADC). Finally, a pure digital electronics card, the FEMINOS board [50], gathers ADC data, performs the pedestal subtraction and sends them to the data acquisition (DAQ) system by means of an ethernet connection.

JCAP12(2015)008

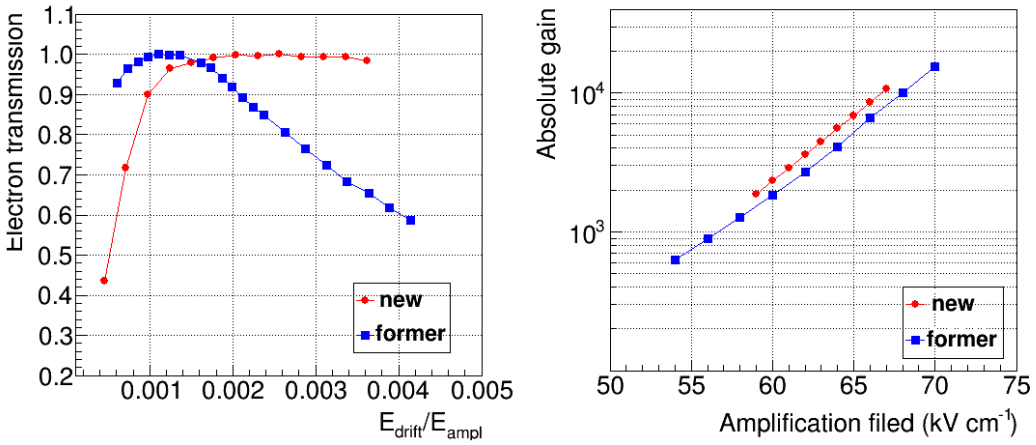

Figure 7. Dependence of the electron transmission on the ratio of drift and amplification fields (left) and of the absolute gain on the amplification field (right) for a new CAST sunrise Micromegas detector (circled red line) and a former design (squared blue line), characterized in Ar+2%iC_4H_{10} at 1.4 bar.

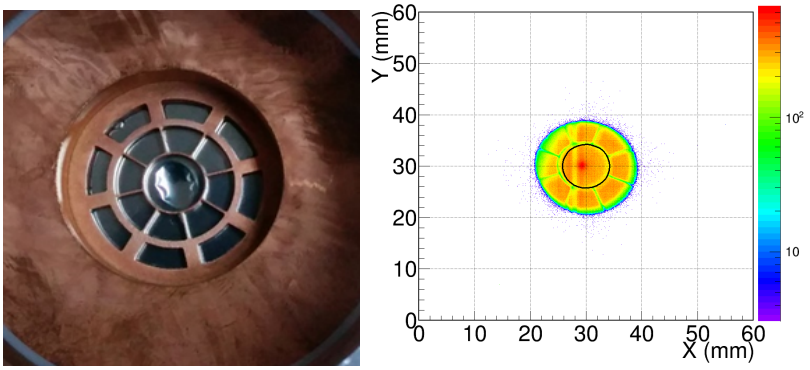

Figure 8. Left: photo of the new copper strongback with the spider web design. Right: intensity plot with the projection of the x-ray window (cathode) in the Micromegas detector during the calibrations.

Special attention has been given to grounding in the electronics design: signal paths are surrounded by a ground layer at the detector, the interface card and the flat cables, to avoid any coupling; the AFTER-based cards and the preamplifier are fixed to the inner part of a Faraday cage to minimize induced noises and each of the high voltage lines has a dedicated low-frequency filter to dim ripples from HV sources.

The 3D reconstruction of an event is made by combining the strip pulses, whose temporal position determines the z axis, and the detector decoding, used for the spatial coordinates, x and y on the detector plane. The charge collection of each event is projected in both spatial and temporal dimensions. As an example, the signals induced on the strips and acquired by the AFTER-based electronics and the resulting yz projection are shown in figure 9.

JCAP12(2015)008

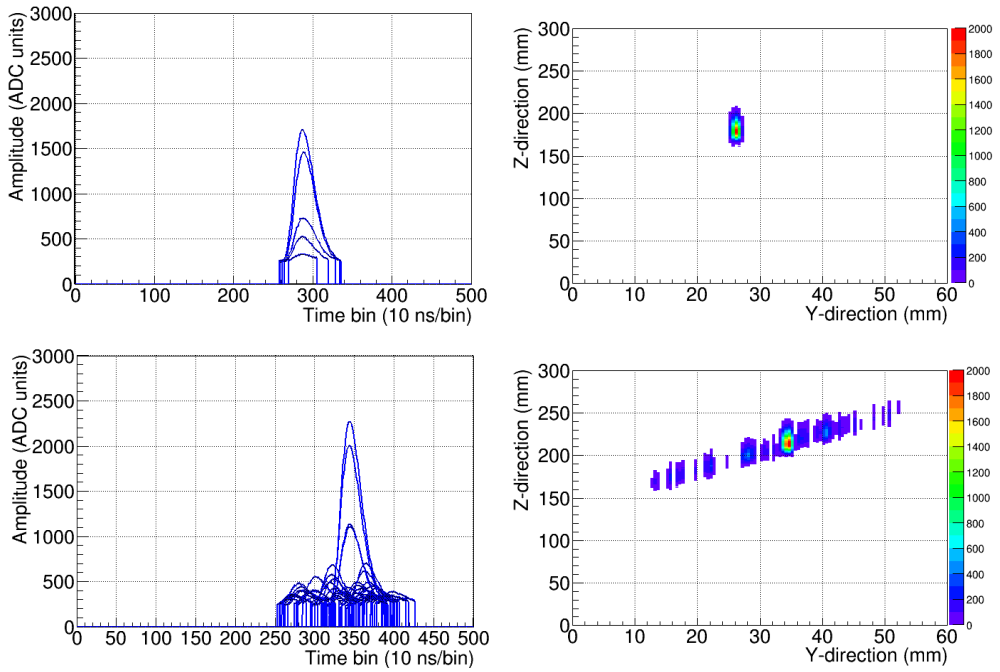

Figure 9. Left: y-strip pulses (recorded in zero-suppression mode) of an x-ray (top) and a background event (bottom) in a CAST Micromegas detector. Right: the yz view of the same events.

5 Installation and commissioning in CAST

The new SRMM detector system was installed at CAST in August 2014. Rough alignment of the optic and its housing was performed using standard surveying techniques to position the optic to within a few mm in the linear horizontal and vertical directions and a few arcminutes in the angular pitch and yaw directions. The next step was to finely align the XRT, using a theodolite to locate a HeNe laser on the bore of the magnet, and using fiducials built into the support structure of the optic. The final step was to insert a diffuser into the visible laser beam, to illuminate the entrance bore of the x-ray telescope. Because a Wolter design is reflective, the optic focuses visible wavelength well (although there is some diffraction). It is therefore possible to compare the measured HeNe transmission at the exit aperture of the x-ray telescope with our ray-trace results. The measurement and simulation are shown in figure 10, and the agreement between the two indicated that the telescope was aligned to better than 30 arcsec to the axis of the magnet bore.

Next, the vacuum components for the differential pumping [44] were installed on either side (elements b, d, e and h of figure 1). The alignment of the Micromegas detector followed, in such a way that the spot be focused at the center of the sensitive area of the detector. In order to accurately fix the position of the detector, a polyethylene support was built. An XY stage was designed as a tailor-made solution to cope with the total weight of the full assembly (∼30 kg) and the moment distribution fixed by geometrical constraints given by the shielding volume and the available room on the detector platform. The alignment was performed with a blank flange at the place of the detector cathode; the flange had a design of the detector's cathode hole-pattern imprinted, on which the parallel laser beam was focused (figure 11, left). When the chamber position was defined, the bolted unions of the XY stage

JCAP12(2015)008

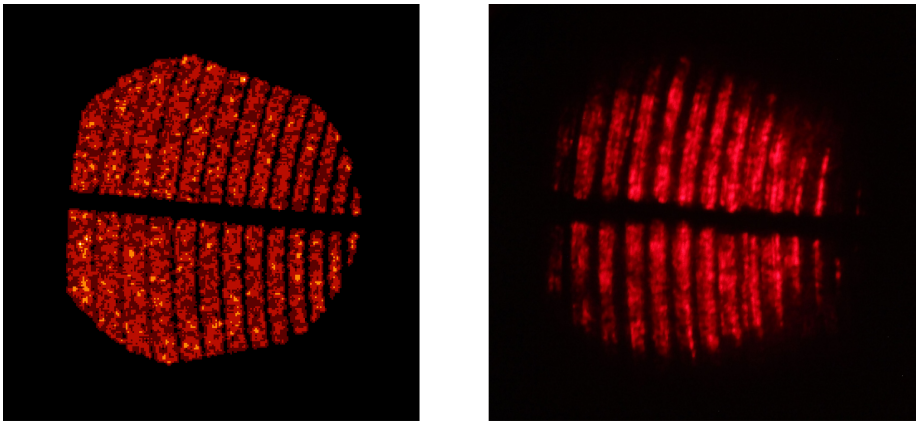

Figure 10. Illumination of the x-ray optic with a HeNe (visible wavelength) laser, after installation and alignment of the telescope into CAST. These images represent the light reflecting and diffracting through the optic, just after the exit aperture. The large gap is due to obscuration by the graphite spacers used to fabricate the optic. Left: simulation based on ray-trace techniques and ad hoc corrections to account for visible wavelength diffraction. Right: photograph of the HeNe laser reflection and diffraction through the optic.

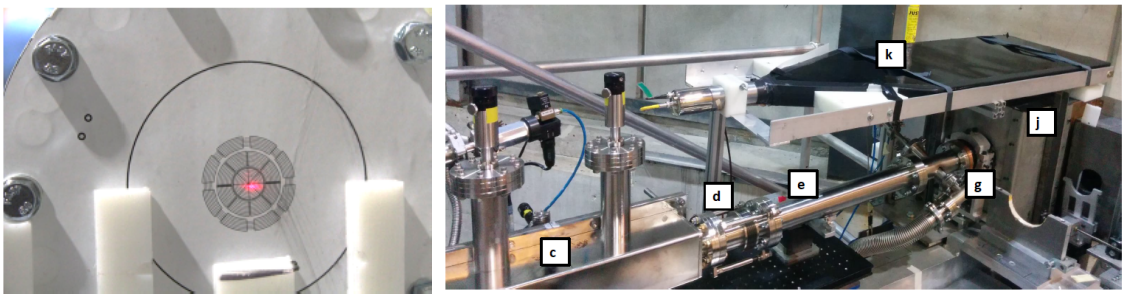

Figure 11. Left: the flange used to align the detector: the laser is focused at the center of the designed pattern, as expected. Right: a picture of the line installed on the CAST platform. The annotated elements follow the description of figure 1.

were locked, fixing thus the position of all line components. Then, the detector replaced the alignment flange and the chamber support was dismounted.

The link between the vacuum line and the detector is made by a 20 mm-thick copper-pipe interface with a PTFE coating. The aperture of the pipe has a diameter of 25 mm. The shielding, consisting of 10 cm of lead, was then built around the detector, leaving only one side at 7 cm because of space constraints. The inner shielding is the detector chamber itself, made of 18 mm radiopure copper. Following the results of extended studies that were carried out [29], a plastic scintillator for the detection of cosmic muons was installed on the top of the shielding. The scintillator covers a part of the pipe that connects the Micromegas with the optic, as external radiation interacting with it is thought to be the source of a significant amount of the background [29]. With the information from the scintillator, the induced x-ray-like events can be discriminated by the off-line analysis. A picture of the installed line can be seen in figure 11, right.

JCAP12(2015)008

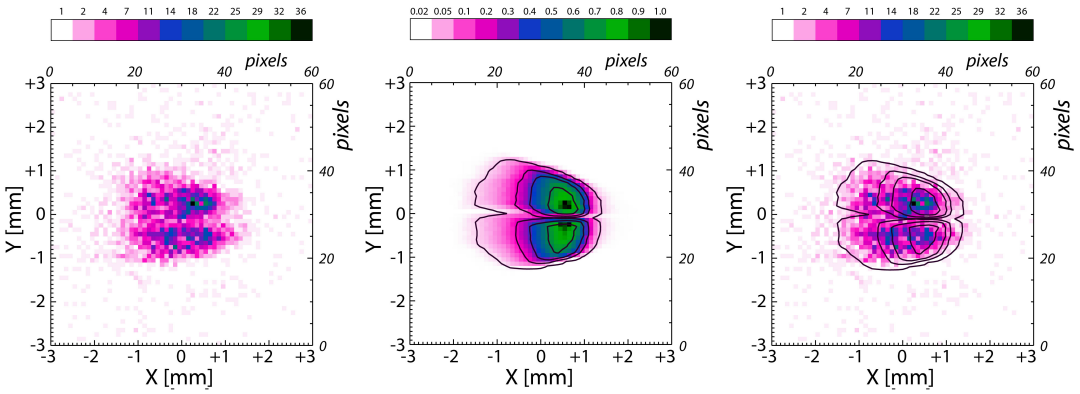

Figure 12. Cool-X x-ray source illumination of the new x-ray telescope. Left: image measured by the Micromegas detector. Middle: simulation, assuming the Cool-X x-ray emission comes from a uniform 6 mm diameter spot. Contour levels are 6%, 30%, 50% and 80% of maximum intensity. Right: data of the Micromegas detector, now with the simulation contours over-plotted.

5.1 Stability of the spot position

The exact knowledge of the position of the spot on the detector is crucial for the data analysis of the experiment, as it defines the area where the expected signal from the axions is to be focused. For this reason, an Amptek Cool-X x-ray generator was installed on the side of the bore opposite of the XRT-Micromegas line (i.e. sunset side of the magnet), with a mechanism able to translate the x-ray source (referred to as the "x-ray finger") from outside the field of view of the XRT, to the central axis of the XRT and magnet bore. Once an operational vacuum level was achieved, the Cool-X was turned on to illuminate the x-ray optic and a long integration was acquired. Figure 12 compares the detector data (left panel) with the ray-tracing simulations (center panel) and then overlays an intensity contour map generated from the ray-tracing results on top the data (right panel). There is excellent agreement between the simulation and measurement, indicating proper alignment and a confirmation of the estimated PSF of the XRT.

The spot position can be periodically monitored performing spot-calibrations with the Cool-X which emits mainly 8 keV photons and bremsstrahlung x-rays. The generator does not produce a constant flux of x-rays but is thermally cycled between 2 to 5 minutes; the flux can vary throughout one cycle and from cycle to cycle. Figure 13 shows the rate recorded by the Micromegas located at the opposite side of the bore and sitting at the back of the x-ray generator, looking for axions during the sunset, compared to the rate of the sunrise detector. The cycles of the generator are evident as well as the 3 orders-magnitude of difference in the recorded rates.

As the source is located at a finite distance to the optic, the spot on the detector plane has a larger diameter than the expected axion signal (see section 3.3). A spot-calibration is presented in figure 14. An intensity map is shown on the left; the energy spectrum acquired during such a calibration is plotted on the right. The higher end of the spectrum is suppressed due to the drop in efficiency of the optic at these energies.

Reference runs with the x-ray finger were performed just after the alignment of the system, before and after the sunrise detector shielding was in place. The low count-rate of the focused spot requires data acquisitions approximately 8 h in duration, in order to collect data with significant statistics. For this reason, spot-calibration runs cannot be taken very

JCAP12(2015)008

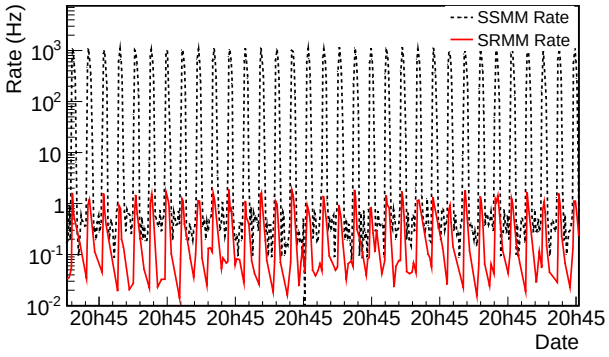

Figure 13. Right: trigger rate in the sunrise Micromegas (SRMM) and the sunset Micromegas (SSMM), during an x-ray finger run.

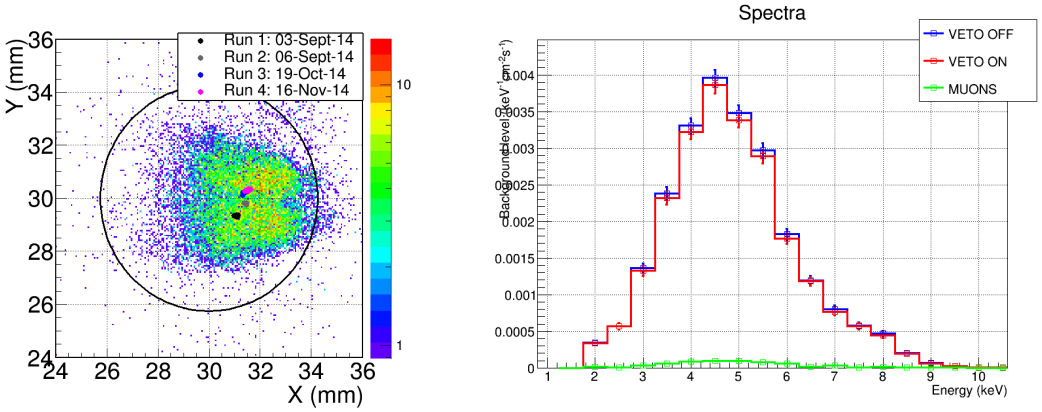

Figure 14. Left: intensity map of the calibration with the x-ray finger through the x-ray optic. The outer contour is the region used (conservatively) to define the background in the spot. Each of the four dots corresponds to the centroid of a spot-calibration with the x-ray finger. Their statistical errors are within the dot size. Right: energy spectrum of an x-ray finger run. The higher end of the spectrum is reduced because of the focusing optic's efficiency loss at these energies.

often so as not to disturb the normal data-taking program of the experiment. Two more spot-calibration runs were performed, one after the installation of the sunset Micromegas detectors and their shielding at the opposite end of the magnet and one after the data taking period, in mid-November 2014. The centroid of the observed spot events has been used to evaluate any possible changes of the spot position during the period of the 2014 data-taking. Table 4 summarizes the measurements. A small shift is observed when adding the shielding around the detector (second calibration) and the shielding around the sunset detectors at the opposite side of the magnet (third calibration). However, only a shift of less than 0.2 mm is observed in either direction (x or y) between the last two spot-calibrations, which represent the positions just before and just after the 2014 data-taking of the experiment.

5.2 Detector performance

The system performance during the ∼50-day data-taking period at the end of 2014 has been stable, as can be seen from the evolution of the monitored parameters like the gain and the energy resolution, plotted in figure 15. Detector calibrations are performed at least twice

JCAP12(2015)008

Year	Run	Time (hours)	Events	Conditions	x-centroid (mm)	y-centroid (mm)
2014	0	9.13	8910	No shielding around detectors	31.09 ± 0.01	29.35 ± 0.01
	1	5.29	4287	Shielding around sunrise MM	31.46 ± 0.01	29.80 ± 0.01
	2	12.43	8617	Shielding around sunset MM	31.34 ± 0.01	30.21 ± 0.01
	3	13.94	7505	End of 2014 data-taking	31.53 ± 0.01	30.30 ± 0.01

Table 4. Details of the four x-ray finger runs taken in 2014 and the corresponding spot positions. The third run corresponds to the beginning of the data-taking period for 2014. Some changes in position are observed with each mounting of the shielding at the two ends of the magnet, however the position of the spot before and after the data-taking did not differ significantly.

a day, once after tracking the Sun in the morning and once during background acquisition. For this purpose, an actuator places an ^{55}Fe source in front of the Micromegas detector and retracts it into a shielded position after the calibration. An imprint of the cathode window strongback can be clearly distinguished during the calibration (figure 8, right). As already mentioned, the size of the window is calculated to cover an area larger than the expected signal spot, the position of which is indicated by a solid black line at the center of the plot.

The data analysis relies on the study of the calibration events, corresponding to x-ray photons of the energy RoI, and the patterns they induce to several observation parameters. These patterns are then compared to the same parameters of the background events. A detailed description can be found in [30]. Events are registered uniformly over the full detector surface (see figure 16); a good part of them has a temporal stamp that coincides with the signal of the muon-veto, labelled "Muons", which are then rejected by the analysis. The background level achieved at a surface covering the calibration area is $(1.6 \pm 0.2)\times10^{-6}$ keV^{-1}cm^{-2}s^{-1}, which with the veto condition applied is reduced to $(1.0 \pm 0.2)\times10^{-6}$ keV^{-1}cm^{-2}s^{-1}.

6 Conclusions and prospects

We have successfully built and commissioned a new low-background x-ray detection line, consisting of a cone-approximation Wolter I x-ray telescope coupled to a shielded Micromegas detector. The telescope is sized to cover the CAST magnet bore (∼5 cm diameter) and has been designed to optimize the signal-to-noise ratio of a detection system in CAST. It assembled from 26 thermally-formed glass substrates, arranged in 13 nested layers, deposited with multilayer coatings. It is the first time an x-ray optic has been designed and built specifically for axion physics. The Micromegas detector is placed at the focal point of the telescope, at a distance of 1.5 m, and is able to image the few mm^2 focal spot expected from solar axions.

The system has been installed and commissioned in one of the two sunrise exits of the CAST magnet in August 2014 and is currently taking data. The installation, commissioning and first calibration data have been described in detail. The expected specifications, in terms of spot size and throughput, agree with first experimental data. The background level of the detector has once more improved over previous designs, reaching a value of $(1.0 \pm 0.2)\times10^{-6}$ keV^{-1}cm^{-2}s^{-1}, the lowest achieved at CAST so far; this value corresponds to 5.4×10^{-3} counts per hour in the energy RoI and signal spot area. This performance translates to the best signal-to-noise ratio by far obtained by any detection system of the

JCAP12(2015)008

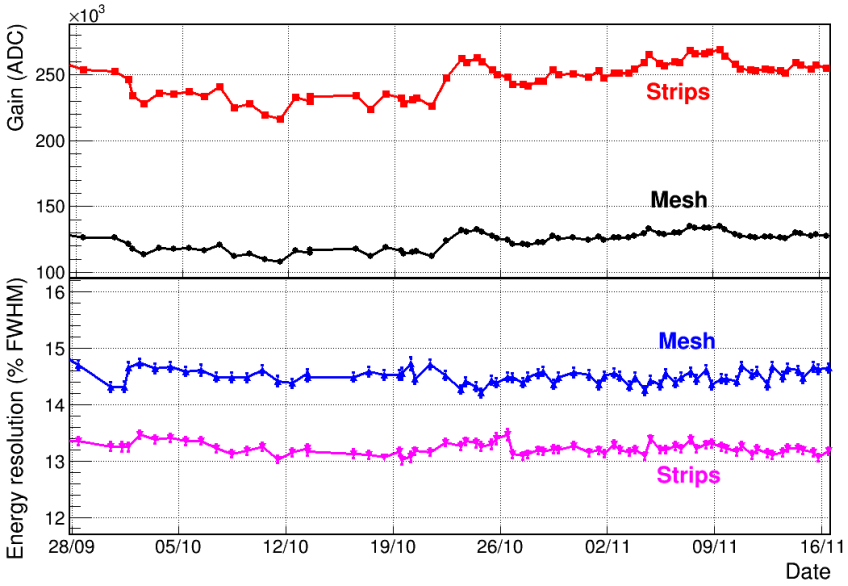

Figure 15. Evolution of the gain and the energy resolution (%FWHM at 5.9 keV) of the detector during the data-taking. The fluctuations, measured both at the mesh and at the strips are less than 5%.

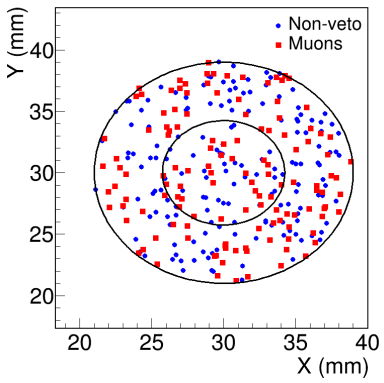

Figure 16. A 2D hitmap of background events in the calibration area (outer circle) with energies between 2 and 14 keV, where the two populations of muon-induced events (muons) and the rest (non-veto) are indicated in red and blue respectively. The inner circle marks the position of the cathode window opening, which includes the spot.

CAST experiment, and will contribute to push the sensitivity of the experiment for the ongoing data taking campaign in 2015.

The system has been conceived as a technological pathfinder for the future International Axion Observatory (IAXO), as it combines two of the techniques (optic and detector) proposed in the conceptual design of the project. It is the first time these two elements are combined and operated together in real data-taking conditions. The operational experience here described is therefore an important milestone in the preparatory phase of IAXO.

JCAP12(2015)008

Acknowledgments

We thank our colleagues at CAST for many years of collaborative work and R. de Oliveira and his team at CERN for the manufacturing of the microbulk readouts. We also thank D. Calvet from CEA/Saclay for his help with the AFTER electronics. We acknowledge the support from the European Commission under the European Research Council T-REX Starting Grant ref. ERC-2009-StG-240054 of the IDEAS program of the 7th EU Framework Program. We also acknowledge support from the Spanish Ministry MINECO under contracts ref. FPA2008-03456 and FPA2011-24058, as well as under the CPAN project ref. CSD2007-00042 from the Consolider-Ingenio 2010 program. These grants are partially funded by the European Regional Development funded (ERDF/FEDER). Part of this work was performed under the auspices of the U.S. Department of Energy by Lawrence Livermore National Laboratory under Contract DE-AC52-07NA27344. F.I. acknowledges the support from the *Juan de la Cierva* program and T.D. from the *Ramón y Cajal* program of MICINN.

References

[1] R.D. Peccei and H.R. Quinn, *CP Conservation in the Presence of Instantons*, *Phys. Rev. Lett.* **38** (1977) 1440 [INSPIRE].

[2] R.D. Peccei and H.R. Quinn, *Constraints Imposed by CP Conservation in the Presence of Instantons*, *Phys. Rev.* **D 16** (1977) 1791 [INSPIRE].

[3] S. Weinberg, *A New Light Boson?*, *Phys. Rev. Lett.* **40** (1978) 223 [INSPIRE].

[4] F. Wilczek, *Problem of Strong p and t Invariance in the Presence of Instantons*, *Phys. Rev. Lett.* **40** (1978) 279 [INSPIRE].

[5] M.S. Turner, *Windows on the Axion*, *Phys. Rept.* **197** (1990) 67 [INSPIRE].

[6] H. Primakoff, *Photo-production of neutral mesons in nuclear electric fields and the mean life of the neutral meson*, *Phys. Rev.* **81** (1951) 899.

[7] P. Sikivie, *Axion cosmology*, *Lect. Notes Phys.* **741** (2008) 19 [astro-ph/0610440] [INSPIRE].

[8] O. Wantz and E.P.S. Shellard, *Axion Cosmology Revisited*, *Phys. Rev.* **D 82** (2010) 123508 [arXiv:0910.1066] [INSPIRE].

[9] H. Baer, A. Lessa and W. Sreethawong, *Coupled Boltzmann calculation of mixed axion/neutralino cold dark matter production in the early universe*, *JCAP* **01** (2012) 036 [arXiv:1110.2491] [INSPIRE].

[10] K.J. Bae, H. Baer and A. Lessa, *Implications of mixed axion/neutralino dark matter for the Cosmic Frontier: a Snowmass whitepaper*, arXiv:1306.2986 [INSPIRE].

[11] A. Arvanitaki, S. Dimopoulos, S. Dubovsky, N. Kaloper and J. March-Russell, *String Axiverse*, *Phys. Rev.* **D 81** (2010) 123530 [arXiv:0905.4720] [INSPIRE].

[12] M. Cicoli, M. Goodsell and A. Ringwald, *The type IIB string axiverse and its low-energy phenomenology*, *JHEP* **10** (2012) 146 [arXiv:1206.0819] [INSPIRE].

[13] A. Ringwald, *Searching for axions and ALPs from string theory*, *J. Phys. Conf. Ser.* **485** (2014) 012013 [arXiv:1209.2299] [INSPIRE].

[14] P. Arias, D. Cadamuro, M. Goodsell, J. Jaeckel, J. Redondo and A. Ringwald, *WISPy Cold Dark Matter*, *JCAP* **06** (2012) 013 [arXiv:1201.5902] [INSPIRE].

[15] IAXO collaboration, I.G. Irastorza, *The International Axion Observatory IAXO. Letter of Intent to the CERN SPS committee*, CERN-SPSC-2013-022 (2013).

JCAP12(2015)008

[16] K. Baker et al., *The quest for axions and other new light particles*, *Annalen Phys.* **525** (2013) A93.

[17] P. Sikivie, *Experimental Tests of the Invisible Axion*, *Phys. Rev. Lett.* **51** (1983) 1415 [*Erratum ibid.* **52** (1984) 695] [INSPIRE].

[18] K. Zioutas et al., *A Decommissioned LHC model magnet as an axion telescope*, *Nucl. Instrum. Meth.* **A 425** (1999) 480 [astro-ph/9801176] [INSPIRE].

[19] CAST collaboration, K. Zioutas et al., *First results from the CERN Axion Solar Telescope (CAST)*, *Phys. Rev. Lett.* **94** (2005) 121301 [hep-ex/0411033] [INSPIRE].

[20] CAST collaboration, S. Andriamonje et al., *An Improved limit on the axion-photon coupling from the CAST experiment*, *JCAP* **04** (2007) 010 [hep-ex/0702006] [INSPIRE].

[21] K. van Bibber, P.M. McIntyre, D.E. Morris and G.G. Raffelt, *A Practical Laboratory Detector for Solar Axions*, *Phys. Rev.* **D 39** (1989) 2089 [INSPIRE].

[22] CAST collaboration, E. Arik et al., *Probing eV-scale axions with CAST*, *JCAP* **02** (2009) 008 [arXiv:0810.4482] [INSPIRE].

[23] CAST collaboration, E. Arik et al., *Search for sub-ev mass solar axions by the cern axion solar telescope with* ^{3}He *buffer gas*, *Phys. Rev. Lett.* **107** (2011) 261302.

[24] CAST collaboration, M. Arik et al., *Search for Solar Axions by the CERN Axion Solar Telescope with* ^{3}*He Buffer Gas: Closing the Hot Dark Matter Gap*, *Phys. Rev. Lett.* **112** (2014) 091302 [arXiv:1307.1985] [INSPIRE].

[25] I.G. Irastorza et al., *Towards a new generation axion helioscope*, *JCAP* **06** (2011) 013 [arXiv:1103.5334] [INSPIRE].

[26] E. Armengaud et al., *Conceptual Design of the International Axion Observatory (IAXO)*, 2014 *JINST* **9** T05002 [arXiv:1401.3233] [INSPIRE].

[27] I. Shilon, A. Dudarev, H. Silva and H.H.J. ten Kate, *Conceptual Design of a New Large Superconducting Toroid for IAXO, the New International AXion Observatory*, *IEEE Trans. Appl. Supercond.* **23** (2013) 4500604 [arXiv:1212.4633] [INSPIRE].

[28] A.C. Jakobsen, M.J. Pivovaroff and F.E. Christensen, *X-ray optics for axion helioscopes*, *Proc. SPIE* **8861** (2013) 886113.

[29] S. Aune et al., *Low background x-ray detection with Micromegas for axion research*, 2014 *JINST* **9** P01001 [arXiv:1310.3391] [INSPIRE].

[30] S. Aune et al., *X-ray detection with Micromegas with background levels below* $10^{-6}\,keV^{-1}cm^{-2}s^{-1}$, 2013 *JINST* **8** C12042 [arXiv:1312.4282] [INSPIRE].

[31] F.A. Harrison et al., *The Nuclear Spectroscopic Telescope Array (NuSTAR) High-Energy X-Ray Mission*, *Astrophys. J.* **770** (2013) 103 [arXiv:1301.7307] [INSPIRE].

[32] M. Kuster et al., *The X-ray Telescope of CAST*, *New J. Phys.* **9** (2007) 169 [physics/0702188] [INSPIRE].

[33] F.A. Harrison et al., *Development of the heft and nustar focusing telescopes*, *Exp. Astron.* **20** (2005) 131.

[34] J.E. Koglin et al., *Nustar hard x-ray optics design and performance*, *Proc. SPIE* 7437 (2009) 74370C.

[35] W.W. Craig et al., *Fabrication of the nustar flight optics*, *Proc. SPIE* **8147** (2011) 81470H.

[36] C.J. Hailey et al., *The nuclear spectroscopic telescope array (nustar): optics overview and current status*, *Proc. SPIE* **7732** (2010) 77320T.

JCAP12(2015)008

[37] R. Petre and P.J. Serlemitsos, *Conical imaging mirrors for high-speed x-ray telescopes*, *Appl. Opt.* **24** (1985) 1833.

[38] A.C. Jakobsen, *X-ray optics for new instruments in astro- and astroparticle physics*, Ph.D. Thesis, Technical University of Denmark, Copenhagen Denmark (2015).

[39] http://www.amptek.com/products/cool-x-pyroelectric-x-ray-generator/.

[40] M.J. Pivovaroff, T. Funk, W.C. Barber, B.D. Ramsey and B.H. Hasegawa, *Progress of focusing x-ray and gamma-ray optics for small animal imaging*, *Proc. SPIE* **5923** (2005) 59230B.

[41] K.K. Madsen et al., *Optimizations of pt/sic and w/si multilayers for the nuclear spectroscopic telescope array*, *Proc. SPIE* **7437** (2009) 743716.

[42] M. Fernandez-Perea et al., *Physics of reflective optics for the soft gamma-ray photon energy range*, *Phys. Rev. Lett.* **111** (2013) 027404.

[43] M.J. Pivovaroff, K.P. Ziock, M. Fernandez-Perea, M.J. Harrison and R. Soufli, *Gamma-ray mirrors for direct measurement of spent nuclear fuel*, *Nucl. Instrum. Meth.* **A 743** (2014) 109.

[44] P. Abbon et al., *The MicrOMEGAs detector of the CAST experiment*, *New J. Phys.* **9** (2007) 170 [physics/0702190] [INSPIRE].

[45] S. Andriamonje et al., *Development and performance of Microbulk MicrOMEGAs detectors*, 2010 *JINST* **5** P02001 [INSPIRE].

[46] F.J. Iguaz, E. Ferrer-Ribas, A. Giganon and I. Giomataris, *Characterization of microbulk detectors in argon- and neon-based mixtures*, 2012 *JINST* **7** P04007 [arXiv:1201.3012] [INSPIRE].

[47] D. Breton, E. Delagnes and M. Houry, *Architecture and implementation of the Front-End Electronics of the Time Projection Chambers in the T2K Experiment*, *IEEE Trans. Nucl. Sci.* **52** (2005) 2853.

[48] P. Baron et al., *AFTER, an ASIC for the readout of the large T2K time projection chambers*, *IEEE Trans. Nucl. Sci.* **55** (2008) 1744 [INSPIRE].

[49] P. Baron et al., *Architecture and implementation of the front-end electronics of the time projection chambers in the T2K experiment*, *IEEE Trans. Nucl. Sci.* **57** (2010) 406 [INSPIRE].

[50] D. Calvet, *A Versatile Readout System for Small to Medium Scale Gaseous and Silicon Detectors*, *IEEE Trans. Nucl. Sci.* **61** (2014) 675 [INSPIRE].

JCAP12(2015)008